PAPER

Check for updates

In situ formed nano-interlayer enables robust interface bonding in efficient Bi₂Te₃-based thermoelectric modules

Rui Zhou,[†a] Ziyan Li,[†b] Shujing Yang,[a] Xuemei Wang,[a] Xinyi Shen,[a] Long Yang,[a] Zhiwei Chen,[a] Juan Chen[*b] and Wen Li [ID] [*a]

Interfacial robustness at thermoelectric–electrode junctions, characterized by exceptional elevated-temperature chemical stability and mechanical integrity, emerges as a critical determinant for the operational longevity of devices. Despite the proven efficacy of barrier layers in mitigating interfacial chemical reaction/diffusion, large-scale fabrication of strongly bonded thermoelectric–barrier–electrode interfaces remains a formidable challenge. In this study, we demonstrate a controllable and reproducible fabrication of Ni electrodes and Ti barrier layers on Bi₂Te₃-based thermoelectric materials *via* an industrially scalable magnetron sputtering process. Impressively, an *in situ* formed nano-interlayer creates atomic bonding at all heterojunctions, achieving an outstanding bonding strength of ∼23 MPa with a competitively low contact resistivity of ∼21 μΩ cm² at the junctions. These eventually enable one-pair thermoelectric modules to achieve a ∼53 K cooling effect at the hot-side temperature of ∼298 K and a sustained ∼4.8% conversion efficiency at a temperature gradient of ∼180 K. This work demonstrates a universal fabrication route for constructing robust interfaces across multiple functional layers in thermoelectric devices.

1. Introduction

Thermoelectric technology, which enables direct heat-to-electricity conversion, has demonstrated promising potential for applications in waste heat recovery, refrigeration systems, and thermal management of optical communication devices.[1] In the past decades, numerous endeavors in thermoelectric materials have driven substantial progress in their performance, with unprecedented enhancements in the dimensionless thermoelectric figure of merit (*zT*).[2] However, the progression of thermoelectric devices, specifically thermoelectric generators, for commercial applications continues to lag conspicuously behind material advances. This disparity is predominantly circumscribed by challenges including insufficient thermal stability under operational conditions and scalability issues in the mass production of the devices.[3]

Thermoelectric devices fundamentally consist of alternating n-and p-type thermoelectric legs interconnected *via* metallic electrodes. The chemical stability of electrode–thermoelectric

junctions at elevated temperatures acts as a critical determinant in governing the long-term performance stability of the devices. It is known that typical weldable electrode materials, including Ni,[4] Ag[5] and Cu,[6] function as efficient dopants in most thermoelectric materials. Interdiffusion between these electrodes and the thermoelectric material generates reaction layers that shift the carrier concentration, degrading thermoelectric properties and increasing contact resistivity over time, thereby lowering conversion efficiency.[7] Therefore, materials exhibiting chemical inertness and a low diffusion coefficient in thermoelectrics have been utilized as intermediate barriers to effectively mitigate such interfacial reactions.[8]

From a mechanical perspective, robust interfacial bonding of electrode–barrier–thermoelectric junctions is indispensable for ensuring device integrity. This constitutes an essential prerequisite for maintaining its long-term operation. The atomic-scale chemical bonds at the interfaces have been demonstrated as an effective strategy to achieve exceptional interfacial strength.[9] However, the facile and scalable fabrication of such robust electrode–barrier–thermoelectric junctions represents a critical challenge to enable commercial viability of thermoelectric generators.

To date, laboratory-scale fabrication of thermoelectric materials integrated with barrier and electrode layers mostly relies on the techniques of hot pressing (HP) or spark plasma sintering (SPS).[10] A mismatch in the coefficients of thermal expansion among these components induces significant

ᵃ*Interdisciplinary Materials Research Center, School of Materials Science and Engineering, Tongji University, Shanghai, 201804, China. E-mail: liwen@tongji.edu.cn*

ᵇ*National Engineering Research Center of Light Alloy Net Forming and State Key Laboratory of Metal Matrix Composite, Shanghai Jiao Tong University, Shanghai, 200240, PR China. E-mail: juanchen@sjtu.edu.cn*

† These authors contribute equally.

internal stresses near the interfaces during the cooling stage after sintering, due to their differential contraction. This results in interfacial shear stress, which poses a risk of delamination, as well as tensile stress that can initiate cracks, thus leading to sintering failure. Commercially, electroplating has been widely used to deposit Ni electrodes in the production of Bi_2Te_3-based thermoelectric devices.[11] However, growing environmental concerns spur significant research efforts toward developing more sustainable and eco-friendly alternatives.

Magnetron sputtering has emerged as a state-of-the-art thin-film deposition technique with universal substrate compatibility and scalability.[12] Such a vacuum-based deposition method offers several unparalleled advantages including exceptional film-substrate adhesion strength, broad material versatility (spanning metals, oxides and nitrides), precise controllability of composition and thickness, and outstanding thickness uniformity.[12b,13] This has been ubiquitously employed for fabricating microelectronic architectures,[14] precision optical and photonic multilayers,[15] advanced surface engineering coatings,[13a,16] energy conversion systems components,[17] biomedical implants interfaces[18] and flexible electronic circuitry.[19] Although this technique has yielded fruitful results in the fundamental research and thin-film preparation of thermoelectric films,[17a,20] its specific application in constructing high-performance dedicated electrodes based on these materials remains an area awaiting further exploration in current research. These findings promote magnetron sputtering as a potential manufacturing paradigm for scalable production of durable electrode–barrier–thermoelectric junctions in thermoelectric devices.

Guided by these critical insights, this work focuses on the magnetron sputtering deposition of Ni electrode monolayers and Ni electrode–Ti barrier bilayers on commercial Bi_2Te_3-based thermoelectric, to meet the exacting interface stability demands in both thermoelectric cooler and generator (Fig. 1a). Both Ni and Ti layers with uniform thickness can be reproducibly fabricated. The nano-interlayers are found to *in situ* form at Ni–Bi_2Te_3 and Ti–Bi_2Te_3 interfaces during processing, which creates atomic-scale interfacial bridging across the junctions. These enable remarkable interfacial bonding strengths of ~23 MPa and ~18 MPa, further accompanied by competitively low interfacial contact resistivities of ~21 mΩ cm^2

and ~31 mΩ cm^2 for the Ni–Bi_2Te_3 and Ti–Bi_2Te_3 interfaces, respectively (Fig. 1b). The highest bonding strength is achieved here as compared to the ever-reported Ni–Bi_2Te_3-based junctions. Eventually, the one-pair thermoelectric modules exhibit a maximum cooling temperature difference of ~53 K at the hot-side temperature of 298 K and a sustained conversion efficiency of ~4.8% under the temperature gradient of 180 K. These findings prove magnetron sputtering as a scalable, industrially compatible deposition technique for the fabrication of electrode–barrier–thermoelectric junctions in robust thermoelectric devices.

2. Results and discussion

Bi_2Te_3-based thermoelectric generators show great promise for low-grade waste heat recovery (<500 K). Ni serves as a standard electrode material for Bi_2Te_3-based thermoelectric coolers, but it undergoes detrimental interfacial reactions with thermoelectric materials at elevated temperatures.[7a,22] Ti has been identified as an effective barrier, successfully suppressing the reaction between Ni electrode and Bi_2Te_3-based thermoelectric.[8b,d,23] In this work, magnetron sputtering is employed to deposit precisely controlled Ni electrode and Ti barrier layers on Bi_2Te_3-based thermoelectric materials, establishing an optimized interfacial architecture for enhanced device stability. Commercial p-type $Bi_{0.5}Sb_{1.5}Te_3$ and n-type $Bi_2Te_{2.7}Se_{0.3}$ thermoelectric materials were procured from Xiamen Xiameritan Technology Company. The detailed layer deposition, characterization, and performance measurements of materials and devices are given in the SI.

The interfacial microstructures of deposited Ni monolayer and Ni–Ti bilayers on both $Bi_{0.5}Sb_{1.5}Te_3$ and $Bi_2Te_{2.7}Se_{0.3}$ were characterized using scanning electron microscopy (SEM), as shown in Fig. 2a, b and S1, respectively. Dense and uniform Ni and Ti layers with thicknesses of ~500 nm and ~300 nm, respectively, are controllably deposited. Continuous interfaces devoid of microscale voids or crack defects indicate good bonding integrity at both Ni/Ti-thermoelectric and Ni–Ti junctions.

Transmission electron microscopy (TEM) observations coupled with energy-dispersive X-ray spectroscopy (EDS) analysis were further performed on Ni–$Bi_{0.5}Sb_{1.5}Te_3$ and Ni–Ti–$Bi_{0.5}Sb_{1.5}Te_3$ junctions for the atomic-scale investigation of the interface morphology, chemical composition, and interdiffusion behavior at the Ni/Ti-thermoelectric and Ni–Ti junctions. Low-magnification TEM image and corresponding EDS mapping reveal clean interfacial transition with well-defined Ni–Ti and Ti–$Bi_{0.5}Sb_{1.5}Te_3$ boundaries, which exhibit no notable elemental enrichment (Fig. 2c).

As shown in Fig. 3a and b, it is remarkably observed that nano-interlayers with thicknesses of 15–20 nm are spontaneously formed at both the Ni–$Bi_{0.5}Sb_{1.5}Te_3$ and Ti–$Bi_{0.5}Sb_{1.5}Te_3$ interfaces. The interlayers contain Ni/Ti, Bi, Sb and Te elements (Fig. S2), with their concentrations gradually varying across the interlayer regions, as evidenced by the EDS line-scan results (insets, Fig. 3a and b). The phase compositions and atomic arrangements of the nano-interlayers are further characterized
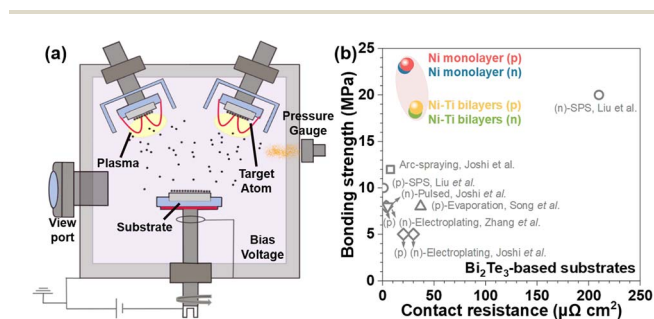

Fig. 1 Schematic of the setup for magnetron sputtering (a), and interfacial contact resistivity and bonding strength for Ni- and Ni–Ti–Bi_2Te_3-based junctions (b), in comparison with literature values.[7a,21]
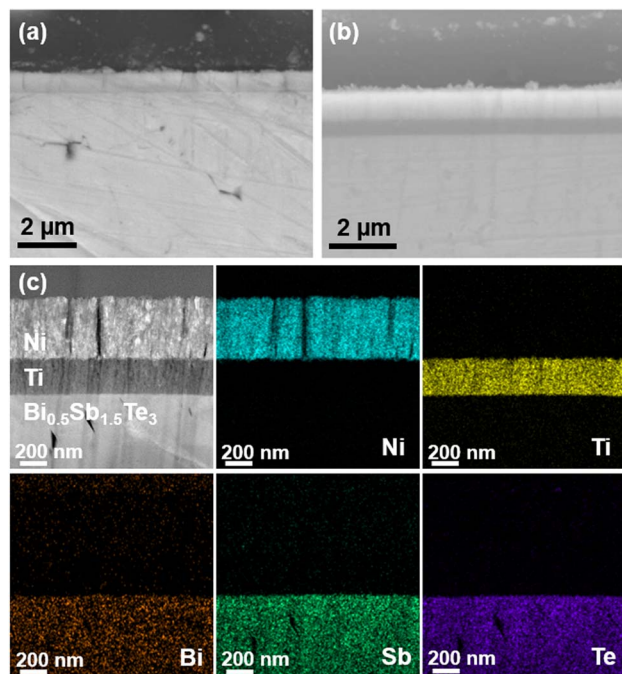
Fig. 2 Scanning electron microscopy (SEM) images of Ni–$Bi_{0.5}Sb_{1.5}Te_3$ (p-type) (a) and Ni–Ti–$Bi_{0.5}Sb_{1.5}Te_3$ (p-type) (b) junctions. Transmission electron microscopy (TEM) image (c) and corresponding energy-dispersive X-ray spectroscopy (EDS) mapping of the Ni–Ti–$Bi_{0.5}Sb_{1.5}Te_3$ junction.
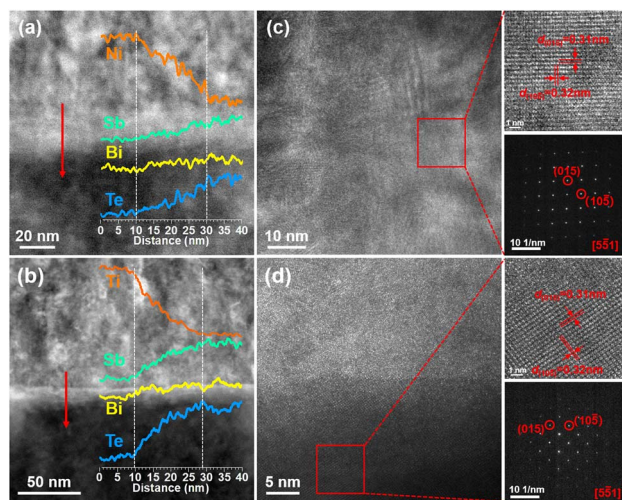

Fig. 3 Low- and high-resolution TEM images (a and b) with corresponding fast Fourier transform (FFT) images (c and d) of Ni–$Bi_{0.5}Sb_{1.5}Te_3$ (a and c) and Ti–$Bi_{0.5}Sb_{1.5}Te_3$ (b and d) interfaces at the Ni–$Bi_{0.5}Sb_{1.5}Te_3$ and Ni–Ti–$Bi_{0.5}Sb_{1.5}Te_3$ junctions. EDS line-scan results are shown as insets in (a) and (b).

by high-resolution TEM observations and fast Fourier transformation (FFT) analyses, as shown in Fig. 3c and d. The phase for the nano-interlayers is revealed to be $Bi_{0.5}Sb_{1.5}Te_3$, crystalizing in a hexagonal structure of the $R\bar{3}m$ space group. This elucidates that there is no detectable formation of intermediate phases between Ni/Ti and $Bi_{0.5}Sb_{1.5}Te_3$ by the magnetron

sputtering process used here. The disordered arrangement near the boundary underscores the incoherent atomic characteristics of the Ni–$Bi_{0.5}Sb_{1.5}Te_3$ and Ti–$Bi_{0.5}Sb_{1.5}Te_3$ interfaces. Similar interfacial behavior has been observed in the Co–MgAgSb junction that achieves extraordinary bonding strength.[9] Moreover, the TEM characterizations on the Ni–Ti interface show the presence of ∼20 nm domains at the phase boundary (Fig. S3a), which are composed of the metallic phases of NiTi alloys (Fig. S3b). All these results indicate the limited interfacial diffusion or reaction at the Ni/Ti–$Bi_{0.5}Sb_{1.5}Te_3$ and Ni–Ti interfaces, suggesting the potentially strong chemical bonding at the heterointerfaces of Ni–$Bi_{0.5}Sb_{1.5}Te_3$, Ti–$Bi_{0.5}Sb_{1.5}Te_3$ and Ni–Ti junctions.

To evaluate the interfacial bonding strength, tensile tests were performed on the Ni–$Bi_{0.5}Sb_{1.5}Te_3$, Ni–$Bi_2Te_{2.7}Se_{0.3}$, Ni–Ti–$Bi_{0.5}Sb_{1.5}Te_3$ and Ni–Ti–$Bi_2Te_{2.7}Se_{0.3}$ junctions. The thermoelectric materials (5 mm × 4 mm × 5 mm) with Ni or Ni–Ti layers deposited on both surfaces were initially adhered to the screws using a high-strength adhesive, as shown in the inset of Fig. 4a. Three independent tensile specimens were prepared for each interfacial junction configuration to ensure statistical reliability. The tests were conducted using a universal testing machine under displacement control at a constant rate of 0.5 mm min^{-1}, which strictly maintained vertical alignment in accordance with ASTM standard.[25]

As shown in Fig. 4a and S4, the average bonding strength for Ni–$Bi_{0.5}Sb_{1.5}Te_3$/$Bi_2Te_{2.7}Se_{0.3}$ junctions reaches ∼23 MPa, representing the highest reported value among all Ni–Bi_2Te_3-based junctions to date (Fig. 1b).[7a,21] In addition, the average bonding strength of ∼18 MPa is achieved in Ni–Ti–$Bi_{0.5}Sb_{1.5}Te_3$/$Bi_2Te_{2.7}Se_{0.3}$ junctions, which is still much higher than most results for similar systems. Fracture surfaces were probed through SEM and EDS characterizations (Fig. S5). The fractures
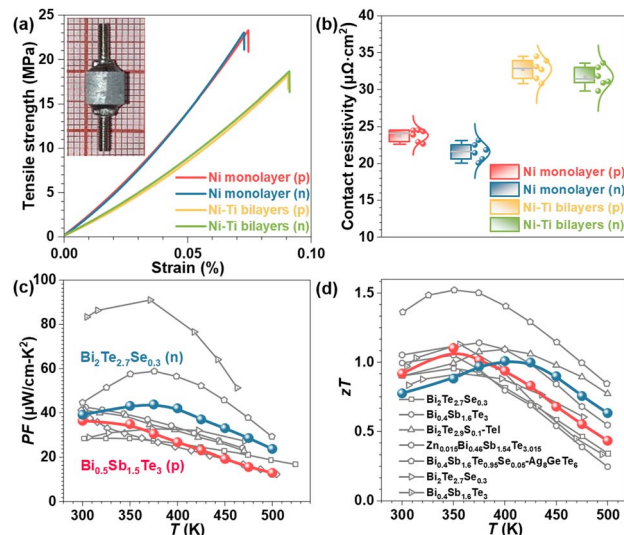

Fig. 4 Tensile stress *versus* strain (a) and interfacial contact resistivity (b) for Ni/Ni–Ti–$Bi_{0.5}Sb_{1.5}Te_3$ and Ni/Ni–Ti–$Bi_2Te_{2.7}Se_{0.3}$ junctions. Power factor PF (c) and zT (d) as a function of temperature for $Bi_{0.5}Sb_{1.5}Te_3$ and $Bi_2Te_{2.7}Se_{0.3}$, in comparison with literature values.[5a,24] Photograph of the tensile test specimen is shown as an inset in (a).

predominantly occur at the Ni/Ti-thermoelectric interfaces, confirming that the measured tensile strengths reflect true interfacial bonding performance.

In addition to the robust interfacial bonding, low interfacial contact resistivity is a critical parameter for determining the power output and conversion efficiency of thermoelectric devices. Here, the interfacial contact resistances (R_c) for various junctions were measured by the four-probe method, and the corresponding results are shown in Fig. 4b and S6–S9. The average R_c from six independent Ni–Bi$_{0.5}$Sb$_{1.5}$Te$_3$ and Ni–Bi$_2$-Te$_{2.7}$Se$_{0.3}$ specimens was found to be 1.46 mΩ and 1.31 mΩ, which correspond to the contact resistivities (ρ_c) of ~23 μΩ cm^2 and ~21 μΩ cm^2, respectively. The Ni–Ti–Bi$_{0.5}$Sb$_{1.5}$Te$_3$ and Ni–Ti–Bi$_2$Te$_{2.7}$Se$_{0.3}$ interfaces exhibit interfacial contact resistivities of ~33 μΩ cm^2 and ~31 μΩ cm^2, respectively. These values are slightly higher than those of Ni–Bi$_{0.5}$Sb$_{1.5}$Te$_3$ and Ni–Bi$_2$Te$_{2.7}$-Se$_{0.3}$ interfaces, which can possibly be understood by the greater work function difference between Ti (4.33 eV) and Bi$_2$Te$_3$ (5.3 eV) than that between Ni (5.15 eV) and Bi$_2$Te$_3$.[26] Nevertheless, all measured interfacial contact resistivities here remain competitive with the ever-reported results (Fig. 1b). Both exceptional interfacial bonding strength and competitive interfacial contact resistivity collectively validate the potential effectiveness of magnetron-sputtered layers in ensuring both exceptional mechanical integrity and power output of the thermoelectric modules.

For further revealing the favorable effect of magnetron-sputtered layers on cooling/generation performance and mechanical integrity, a thermoelectric cooler was assembled using single-pair Ni–Bi$_{0.5}$Sb$_{1.5}$Te$_3$ (p) and Ni–Bi$_2$Te$_{2.7}$Se$_{0.3}$ (n) legs (1.6 mm × 2 mm × 5.5 mm and 1.6 mm × 1.6 mm × 5.5 mm), while a thermoelectric generator was constructed with Ni–Ti–Bi$_{0.5}$Sb$_{1.5}$Te$_3$ (p) and Ni–Ti–Bi$_2$Te$_{2.7}$Se$_{0.3}$ (n) legs (1.6 mm × 1.6 mm × 5 mm and 2 mm × 1.9 mm × 5 mm). Systematic transport property measurements were performed on commercial Bi$_{0.5}$Sb$_{1.5}$Te$_3$ and Bi$_2$Te$_{2.7}$Se$_{0.3}$ thermoelectric materials (Fig. S10). These materials exhibit room-temperature power factors of ~36 μW cm^{-1} K^{-2} and ~39 μW cm^{-1} K^{-2} (Fig. 4c), with zT values of ~0.9 and ~0.77 (Fig. 4d), respectively. Finite element simulation incorporating leg geometry optimization was performed to achieve the ideal maximum cooling temperature difference (ΔT_{max}) based on the materials' thermoelectric properties (Fig. S11a).[27] The hot-side temperature is fixed at 298 K. An ΔT_{max} of ~53 K is achieved for the cooler at an optimized current, as shown in Fig. 5a, b and S11b. The obtained ΔT_{max} shows excellent agreement with theoretical prediction considering interfacial resistances, achieving ~95% of the ideal ΔT_{max} predicted for resistance-free interfaces (Fig. 5b).

Furthermore, the performance of the thermoelectric generator is measured under a fixed cold-side temperature of 290 K (Fig. 5c, d and S12). The output voltage (V) exhibits a linear dependence on current across different temperature gradient (ΔT), with the intercept and slope corresponding to the open-circuit voltage (V_{oc}) and internal resistance (R_{in}), respectively (Fig. 5c). Both V_{oc} and R_{in} show a positive correlation with ΔT. The increase in V_{oc} originates from the increased Seebeck
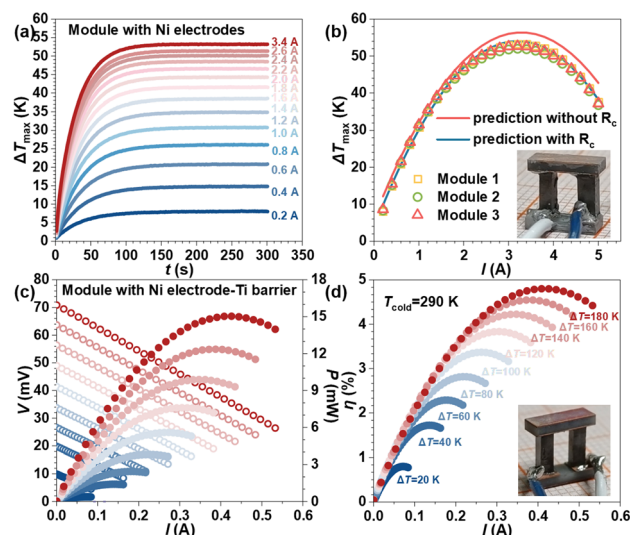
Fig. 5 Maximum cooling temperature difference (DT_{max}) as function of time t (a) and current I (b) for Ni-Bi$_{0.5}$Sb$_{1.5}$Te$_3$ (p-type) and Ni-Bi$_2$-Te$_{2.7}$Se$_{0.3}$ (n-type) thermoelectric cooler at a hot-side temperature of 298 K, with a comparison to the theoretical predictions. Output voltage and power (c) and conversion efficiency (d) as a function of current for Ni-Ti-Bi$_{0.5}$Sb$_{1.5}$Te$_3$ (p-type) and Ni-Ti-Bi$_2$Te$_{2.7}$Se$_{0.3}$ (n-type) thermoelectric generator at various temperature gradient. Photographs of thermoelectric cooler and generator are shown as the insets in (b) and (d), respectively.

coefficient of the materials below 400 K and the growing ΔT at higher temperatures (Fig. S10a). The rise in R_{in} primarily results from the increasing electrical resistivity of the materials (Fig. S10b). Ultimately, a maximum P_{max} of ~16.8 mW and a maximum conversion efficiency (η_{max}) of ~4.8% are achieved at a ΔT of 180 K. These results demonstrate Bi$_2$Te$_3$-based thermoelectric generators as a promising sustainable energy technology for low-grade waste heat recovery ($T < 500$ K).

The obtained η_{max} at different ΔT for the thermoelectric generator in this work is found to rank among the highest reported Bi$_2$Te$_3$-based thermoelectric generators[5a,24] (Fig. 6a). The long-term measurements, shown in Fig. 6b, reveal no observable degradation in V_{oc}, P_{max} and η_{max} for Ni–Ti–Bi$_{0.5}$Sb$_{1.5}$Te$_3$ (p) and Ni–Ti–Bi$_2$Te$_{2.7}$Se$_{0.3}$ (n) thermoelectric generator. These
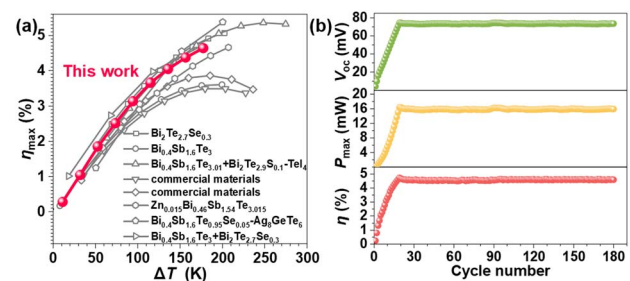
Fig. 6 Maximum conversion efficiency (η_{max}) for Ni–Ti–Bi$_{0.5}$Sb$_{1.5}$Te$_3$ (p) and Ni–Ti–Bi$_2$Te$_{2.7}$Se$_{0.3}$ (n) thermoelectric generators at various temperature gradients, in comparison with literature values[5a,24] (a). Open-circuit voltage (V_{oc}), maximum output power (P_{max}) and η_{max} during the long-term measurements (b).

results conclusively demonstrate the exceptional mechanical integrity of the magnetron-sputtered electrode–barrier–thermoelectric interfaces, which is crucial for ensuring reliable long-term generator operation at elevated operating temperatures.

3. Summary

In summary, an industrial-compatible technique of magnetron sputtering enables a reproducible and controllable fabrication of Ni electrode monolayer and Ni electrode–Ti barrier bilayers on Bi_2Te_3-based thermoelectric materials. The *in situ* formed nano-interlayers at the interfaces create atomic bonding of the heterojunctions, yielding superior interfacial bonding strength (>18 MPa). Such interfacial bonding achieves competitively low interfacial contact resistivities of <24 $\mu\Omega$ cm^2 and <33 $\mu\Omega$ cm^2 for Ni electrode-/Ti barrier-thermoelectric junctions, respectively. Both competitive interfacial resistivity and exceptional bonding strength guarantee the achievements of a cooling temperature difference of ~53 K at the hot-side temperature of ~298 K and a durable conversion efficiency of ~4.8% at the temperature gradient of ~180 K. This work strongly demonstrates the robustness of magnetron-sputtered electrode–barrier–thermoelectric interfaces for ensuring mechanical integrity with low interfacial resistivity of the thermoelectric generators, providing new perspectives for the scalable fabrications of electrode and barrier layers in other thermoelectric material systems.

Data availability

The data are also available from the corresponding authors upon request.

The data that support the findings of this study are included in the main article and SI. Supplementary information : materials and methods details; SEM/TEM images and EDS elemental mapping for the Ni-$Bi_{0.5}Sb_{1.5}Te_3$ and Ti-$Bi_{0.5}Sb_{1.5}Te_3$ junctions; tensile stress versus strain curves for the junctions; measurements of the interfacial contact resistance for six junction specimens; the thermoelectric properties of the materials; theoretical simulations of the cooling performance for a single-pair module; and output performance testing of the power generation module. See DOI: https://doi.org/10.1039/d5ta06391d.

Conflicts of interest

The authors declare no conflict of interest.

Acknowledgements

References

1 (*a*) X. F. Zheng, C. X. Liu, Y. Y. Yan and Q. Wang, *Renewable Sustainable Energy Rev.*, 2014, **32**, 486; (*b*) W. Y. Chen, X. L. Shi, J. Zou and Z. G. Chen, *Small Methods*, 2022, **6**, 2101235; (*c*) S. M. Pourkiaei, M. H. Ahmadi, M. Sadeghzadeh, S. Moosavi, F. Pourfayaz, L. Chen, M. A. Pour Yazdi and R. Kumar, *Energy*, 2019, **186**, 115849; (*d*) D. Beretta, N. Neophytou, J. M. Hodges, M. G. Kanatzidis, D. Narducci, M. Martin- Gonzalez, M. Beekman, B. Balke, G. Cerretti, W. Tremel, A. Zevalkink, A. I. Hofmann, C. Müller, B. Dörling, M. Campoy-Quiles and M. Caironi, *Mater. Sci. Eng., R*, 2019, **138**, 100501.

2 (*a*) X. Wang, Z. Chen, S. Zhang, X. Zhang, R. Zhou, W. Li, J. Luo and Y. Pei, *InfoMat*, 2025, **7**, e12663; (*b*) B. Zhu, X. Liu, Q. Wang, Y. Qiu, Z. Shu, Z. Guo, Y. Tong, J. Cui, M. Gu and J. He, *Energy Environ. Sci.*, 2020, **13**, 2106; (*c*) W.-D. Liu, L.-C. Yin, L. Li, Q. Yang, D.-Z. Wang, M. Li, X.-L. Shi, Q. Liu, Y. Bai, I. Gentle, L. Wang and Z.-G. Chen, *Energy Environ. Sci.*, 2023, **16**, 5123; (*d*) X. Qi, T. Kang, L. Yang, X. Zhang, J. Luo, W. Li and Y. Pei, *Adv. Sci.*, 2024, **11**, 2407413; (*e*) J. Zhou, Z. Chen, J. Luo, W. Li and Y. Pei, *Adv. Mater.*, 2024, **36**, 2405299; (*f*) Z. Bu, X. Zhang, Y. Hu, Z. Chen, S. Lin, W. Li, C. Xiao and Y. Pei, *Nat. Commun.*, 2022, **13**, 237.

3 (*a*) C. Fu, S. Bai, Y. Liu, Y. Tang, L. Chen, X. Zhao and T. Zhu, *Nat. Commun.*, 2015, **6**, 8144; (*b*) Q. Zhang, J. Liao, Y. Tang, M. Gu, C. Ming, P. Qiu, S. Bai, X. Shi, C. Uher and L. Chen, *Energy Environ. Sci.*, 2017, **10**, 956.

4 (*a*) K. Xiong, W. Wang, H. N. Alshareef, R. P. Gupta, J. B. White, B. E. Gnade and K. Cho, *J. Phys. D: Appl. Phys.*, 2010, **43**, 115303; (*b*) W. Zhu, P. Wei, J. Zhang, L. Li, W. Zhu, X. Nie, X. Sang, Q. Zhang and W. Zhao, *ACS Appl. Mater. Interfaces*, 2022, **14**, 12276; (*c*) X. R. Ferreres, S. Aminorroaya Yamini, M. Nancarrow and C. Zhang, *Mater. Des.*, 2016, **107**, 90.

5 (*a*) L. Yin, F. Yang, X. Bao, W. Xue, Z. Du, X. Wang, J. Cheng, H. Ji, J. Sui, X. Liu, Y. Wang, F. Cao, J. Mao, M. Li, Z. Ren and Q. Zhang, *Nat. Energy*, 2023, **8**, 665; (*b*) H.-T. Liu, Q. Sun, Y. Zhong, Q. Deng, L. Gan, F.-L. Lv, X.-L. Shi, Z.-G. Chen and R. Ang, *Nano Energy*, 2022, **91**, 106706; (*c*) H. Geng, H. Zhu, Z. Deng and Y. Qu, *Solid State Sci.*, 2025, **160**, 107785.

6 (*a*) L.-C. Yin, W.-D. Liu, M. Li, D.-Z. Wang, H. Wu, Y. Wang, L. Zhang, X.-L. Shi, Q. Liu and Z.-G. Chen, *Adv. Funct. Mater.*, 2023, **33**, 2301750; (*b*) L. Xu, X. Wang, Y. Wang, Z. Gao, X. Ding and Y. Xiao, *Energy Environ. Sci.*, 2024, **17**, 2018; (*c*) R. Deshpande, A. Bahrami, F. Kreps, R. He, P. Ying, K. Nielsch, E. Müller and J. de Boor, *ACS Appl. Mater. Interfaces*, 2025, **17**, 28777; (*d*) R. O. Carlson, *J. Phys. Chem. Solids*, 1960, **13**, 65; (*e*) S. Fujimoto, S. Sano and T. Kajitani, *Jpn. J. Appl. Phys.*, 2007, **46**, 5033.

7 (*a*) W. Liu, H. Wang, L. Wang, X. Wang, G. Joshi, G. Chen and Z. Ren, *J. Mater. Chem. A*, 2013, **1**, 13093; (*b*) Z.-k. Hu and S.-w. Chen, *J. Alloys Compd.*, 2022, **899**, 163299; (*c*) C. C. Li,

F. Drymiotis, L. L. Liao, H. T. Hung, J. H. Ke, C. K. Liu, C. R. Kao and G. J. Snyder, *J. Mater. Chem. C*, 2015, **3**, 10590; (*d*) W. Liu, Q. Jie, H. S. Kim and Z. Ren, *Acta Mater.*, 2015, **87**, 357; (*e*) W.-S. Liu, Y. Liu, F. Zhao, S.-M. Zhang and X.-K. Hu, *J. Inorg. Mater.*, 2019, **34**, 269; (*f*) J. Navrátil, I. Klichová, S. Karamazov, J. Srámková and J. Horák, *J. Solid State Chem.*, 1998, DOI: 10.1006/jssc.1998.7818; (*g*) A. Vaško, L. Tichý, J. Horák, *et al*, *Appl. Phys.*, 1974, **5**, 217–221.

8 (*a*) M. Liu, X. Zhang, W. Ding and Y. Pei, *ACS Appl. Mater. Interfaces*, 2024, **16**, 31826; (*b*) M. Liu, X. Zhang, S. Hu, R. Zhou, Y. Guo and W. Li, *ACS Appl. Mater. Interfaces*, 2025, **17**, 28873; (*c*) C.-H. Wang, H.-C. Hsieh, Z.-W. Sun, V. K. Ranganayakulu, T.-W. Lan, Y.-Y. Chen, Y.-Y. Chang and A. T. Wu, *ACS Appl. Mater. Interfaces*, 2020, **12**, 27001; (*d*) M. Liu, W. Li and Y. Pei, *Sci. China Mater.*, 2024, **67**, 289; (*e*) S. Hu, M. Liu, L. Yang, Z. Chen, J. Luo, W. Li and Y. Pei, *J. Power Sources*, 2025, **630**, 236102; (*f*) H. Pan, L. Zhang, H. Geng, Q. Chang, B. Zhang and Z. Sun, *Mater. Today Phys.*, 2025, **50**, 101635.

9 W. Zuo, H. Chen, Z. Yu, Y. Fu, X. Ai, Y. Cheng, M. Jiang, S. Wan, Z. Fu, R. Liu, G. Cheng, R. Xu, L. Wang, F. Xu, Q. Zhang, D. Makarov and W. Jiang, *Nat. Mater.*, 2025, **24**, 735.

10 (*a*) Z. Wu, S. Zhang, Z. Liu, E. Mu and Z. Hu, *Nano Energy*, 2022, **91**, 106692; (*b*) Q. Yan and M. G. Kanatzidis, *Nat. Mater.*, 2021, **21**, 503; (*c*) Y. N. Nguyen, S. Kim, S. H. Bae and I. Son, *Appl. Surf. Sci.*, 2021, **545**, 149005.

11 (*a*) L. Chen, D. Mei, Y. Wang and Y. Li, *J. Alloys Compd.*, 2019, **796**, 314; (*b*) H. Zhang, P. Wei, C. Zhou, L. Li, X. Nie, W. Zhu and W. Zhao, *J. Mater. Sci.: Mater. Electron.*, 2024, **35**, 727; (*c*) F. Giulio, A. Mazzacua, L. Calciati and D. Narducci, *Materials*, 2024, **17**, 1549.

12 (*a*) T. Eleutério, S. Sério and H. C. Vasconcelos, *Coatings*, 2023, **13**, 922; (*b*) C. Yin, T. Zhang, C. Zhang, Y. Zhang, C. K. Jeong, G. T. Hwang and Q. Chi, *SusMat*, 2024, **4**, e228; (*c*) D. Carreira, P. Ribeiro, M. Raposo and S. Sério, *Photonics*, 2021, **8**, 75.

13 (*a*) J. Zheng, Z. Huang, Y. Zeng, W. Liu, B. Wei, Z. Qi, Z. Wang, C. Xia and H. Liang, *Nano Lett.*, 2022, **22**, 1017; (*b*) B. Meng, J. Wang, M. Chen, S. Zhu and F. Wang, *Corros. Sci.*, 2023, **225**, 111591; (*c*) A. Barranco, A. Borras, A. R. Gonzalez-Elipe and A. Palmero, *Prog. Mater. Sci.*, 2016, **76**, 59; (*d*) Y. Xu, J. Zhang, F. Liang, M. Yin and M. He, *Surf. Interfaces*, 2023, **38**, 102770.

14 (*a*) S. Kodan, A. Kumar, A. Sanger, A. Arora, V. K. Malik and R. Chandra, *Sens. Actuators, B*, 2024, **407**, 135481; (*b*) H. Ye, Z. Tu and S. Li, *J. Power Sources*, 2024, **595**, 234052; (*c*) S. Li, J. Liang, P. Wei, Q. Liu, L. Xie, Y. Luo and X. Sun, *eScience*, 2022, **2**, 382.

15 (*a*) L.-X. Qian, Z.-H. Wu, Y.-Y. Zhang, P. T. Lai, X.-Z. Liu and Y.-R. Li, *ACS Photonics*, 2017, **4**, 2203; (*b*) F. Wu, X. Wu, S. Xiao, G. Liu and H. Li, *Opt. Express*, 2021, **29**, 23976; (*c*) L. Dong, R. Jia, B. Xin, B. Peng and Y. Zhang, *Sci. Rep.*, 2017, **7**, 40160; (*d*) N. Sagara, S. Kamimura, T. Tsubota and T. Ohno, *Appl. Catal., B*, 2016, **192**, 193.

16 (*a*) C. Yin, T. Zhang, C. Zhang, Y. Zhang, C. K. Jeong, G.-T. Hwang and Q. Chi, *SusMat*, 2024, **4**, e228; (*b*) Y. Ma, Y. Du, Y. Chen, C. Gu, T. Jiang, G. Wei and J. Zhou, *Chem. Eng. J.*, 2020, **381**, 122710; (*c*) B. Meng, J. Wang, M. Chen, S. Zhu and F. Wang, *Corros. Sci.*, 2023, **225**, 111591.

17 (*a*) B. Hinterleitner, I. Knapp, M. Poneder, Y. Shi, H. Müller, G. Eguchi, C. Eisenmenger-Sittner, M. Stöger-Pollach, Y. Kakefuda, N. Kawamoto, Q. Guo, T. Baba, T. Mori, S. Ullah, X.-Q. Chen and E. Bauer, *Nature*, 2019, **576**, 85; (*b*) K. Zhou, M. Zhao, X. Meng, Y. Wei, J. Zhu, X. Sun and Z. Ma, *Ceram. Int.*, 2024, **50**, 27120; (*c*) M. Dc, R. Grassi, J.-Y. Chen, M. Jamali, D. Reifsnyder Hickey, D. Zhang, Z. Zhao, H. Li, P. Quarterman, Y. Lv, M. Li, A. Manchon, K. A. Mkhoyan, T. Low and J.-P. Wang, *Nat. Mater.*, 2018, **17**, 800.

18 (*a*) W. Liu, J. Li, M. Cheng, Q. Wang, K. W. K. Yeung, P. K. Chu and X. Zhang, *Adv. Sci.*, 2018, **5**, 1800749; (*b*) M. Li, L. Li, K. Su, X. Liu, T. Zhang, Y. Liang, D. Jing, X. Yang, D. Zheng, Z. Cui, Z. Li, S. Zhu, K. W. K. Yeung, Y. Zheng, X. Wang and S. Wu, *Adv. Sci.*, 2019, **6**, 1900599; (*c*) H. Shokrollahi, *J. Magn. Magn. Mater.*, 2017, **426**, 74; (*d*) J. Dong, X. Tang, Y. Peng, C. Fan, L. Li, C. Zhang, F. Lai, G. He, P. Ma, Z. Wang, Q. Wei, X.-P. Yan, H.-L. Qian, Y. Huang and T. Liu, *Nano Energy*, 2023, **108**, 108194.

19 (*a*) D. Yang, R. Yang, J. Zhang, Z. Yang, S. Liu and C. Li, *Energy Environ. Sci.*, 2015, **8**, 3208; (*b*) Z. Zhang, L. Wu, D. Zhou, W. Weng and X. Yao, *Nano Lett.*, 2021, **21**, 5233; (*c*) S. Wang, B. Xu, W. Huo, H. Feng, X. Zhou, F. Fang, Z. Xie, J. K. Shang and J. Jiang, *Appl. Catal., B*, 2022, **313**, 121472.

20 (*a*) I. R. Bekpulatov, V. V. Loboda, M. T. Normuradov, B. D. Donaev and I. K. Turapov, *Phys. Mater. Technol.*, 2023, **16**(2), 163; (*b*) F. Amirghasemi and S. Kassegne, *J. Electron. Mater.*, 2021, **50**, 2190; (*c*) Y. Shao, P. Zheng, T. Dong, L. Wei, H. Wu and J. Si, *Vacuum*, 2024, **220**, 112791.

21 (*a*) G. Joshi, D. Mitchell, J. Ruedin, K. Hoover, R. Guzman, M. McAleer, L. Wood and S. Savoy, *J. Mater. Chem. C*, 2019, **7**, 479; (*b*) E. Song, B. S. Swartzentruber, C. R. Koripella and J. A. Martinez, *ACS Omega*, 2019, **4**, 9376; (*c*) J. Zhang, P. Wei, H. Zhang, L. Li, W. Zhu, X. Nie, W. Zhao and Q. Zhang, *ACS Appl. Mater. Interfaces*, 2023, **15**, 22705.

22 (*a*) K.-W. Cheng, C.-H. Kung, J.-Y. Huang, C.-H. Ku, Q.-M. Huang, V. K. Ranganayakulu, Y.-Y. Chen, S.-J. Chiu, Y.-G. Lin, C.-M. Wang and A. T. Wu, *Mater. Chem. Phys.*, 2024, **318**, 129208; (*b*) Y. Geng, H. He, R. Liang, Q. Lai, L. Hu, F. Liu and C. Zhang, *Adv. Energy Mater.*, 2024, **14**, 2402479; (*c*) C. Fang, G. Chen, Z. Li, X. Wang, B. Duan, X. Feng, G. Li and P. Zhai, *J. Mater. Sci.: Mater. Electron.*, 2025, **36**, 200.

23 (*a*) A. Katsura, M. Tsurumoto, A. Suetake, Y. Hirose, D. Micucci and T. Sugahara, *AIP Adv.*, 2025, **15**, 035351; (*b*) M. Liu, W. Li and Y. Pei, *Sci. China Mater.*, 2023, **67**, 289.

24 (*a*) J. M. Park, D. Y. Hyeon, H.-S. Ma, S. Kim, S.-T. Kim, Y. N. Nguyen, I. Son, S. Yi, K. T. Kim and K.-I. Park, *J. Alloys Compd.*, 2021, **884**, 161119; (*b*) Y. K. Zhu, Y. Sun, J. Zhu, K. Song, Z. Liu, M. Liu, M. Guo, X. Dong, F. Guo, X. Tan, B. Yu, W. Cai, J. Jiang and J. Sui, *Small*, 2022, **18**,

2201352; (*c*) R. Deng, X. Su, S. Hao, Z. Zheng, M. Zhang, H. Xie, W. Liu, Y. Yan, C. Wolverton, C. Uher, M. G. Kanatzidis and X. Tang, *Energy Environ. Sci.*, 2018, **11**, 1520; (*d*) J. Qiu, Y. Yan, T. Luo, K. Tang, L. Yao, J. Zhang, M. Zhang, X. Su, G. Tan, H. Xie, M. G. Kanatzidis, C. Uher and X. Tang, *Energy Environ. Sci.*, 2019, **12**, 3106; (*e*) T. Lu, B. Wang, G. Li, J. Yang, X. Zhang, N. Chen, T.-H. Liu, R. Yang, P. Niu, Z. Kan, H. Zhu and H. Zhao, *Mater. Today Phys.*, 2023, **32**, 101035; (*f*) Q. Zhang, M. Yuan, K. Pang, Y. Zhang, R. Wang, X. Tan, G. Wu, H. Hu, J. Wu, P. Sun, G.-Q. Liu and J. Jiang, *Adv. Mater.*, 2023, **35**, 2300338.

25 *Annual Book of ASTM Standards*, ASTM International, West Conshohocken, PA, 2015, DOI: **10.1520/e0008_e0008m-16a**.

26 (*a*) B. Ryu, *J. Korean Phys. Soc.*, 2018, **72**, 122; (*b*) D. Haneman, *J. Phys. Chem. Solids*, 1959, **11**, 205; (*c*) P. Villars, and F. Hulliger, *Ti RT work function: Datasheet from "PAULING FILE Multinaries Edition – 2022*, Springer-Verlag Berlin Heidelberg & Material Phases Data System (MPDS), Switzerland & National Institute for Materials Science (NIMS), Japan, 2011.

27 (*a*) W.-H. Chen, C.-Y. Liao and C.-I. Hung, *Appl. Energy*, 2012, **89**, 464; (*b*) M. Hodes, *IEEE Trans. Comp. Pack. Technol.*, 2007, **30**, 50.